Numerical simulation and optimization of the ceramic pigments production process by using microwave heating

Pedro André Varela Ramos
pedro.v.ramos@tecnico.ulisboa.pt

Instituto Superior Técnico, Universidade de Lisboa, Portugal

February 2021

Abstract

Ceramic pigments are widely used to give colour in several industries. The high temperatures that characterize the pigment formation make this sector a very energy intensive one, contributing to greenhouse gas emissions if conventional heating is used.
In this study, the continuous microwave production of pigments was modelled using *COMSOL Multiphysics* together with a controller developed in *MATLAB* to automatically manage the input power and the cavity impedance. A single-mode cavity operating at 2.45 GHz, together with a rectangular waveguide, was used. A chemical model using experimental data was developed using a model-fitting approach to predict chemical conversion with time. The mathematical model includes a two-way coupling between Maxwell's equations and heat equation as well as coupling between thermal and chemical interfaces.
A parametric study including variation in velocity and convection coefficient was also performed to evaluate the impact of these variables in the efficiency of the process. Attenuation occurs significantly within the material as dielectric properties are high. As such, prohibitive temperatures can be attained easily if the input power is not controlled properly. Electromagnetic efficiency is highly dependent on the thermal field, making the boundary convection coefficient the parameter that affects the most the electromagnetic heating performance. Thermal conductivity is also a crucial parameter that can contribute to attenuation and superficial heating. To show the influence of physical properties in the heating mechanism two pigments were used in the simulations.

Keywords: Ceramic pigments continuous production, High temperature microwave heating, Multiphysics numerical simulation, Efficiency optimization, Input power control.

1. Introduction

Pigments are solid and insoluble substances that give tone (whether it is a coloured, black or white tone) and/or protection to a medium [1]. Alocromatic pigments, as known as solid solutions, are one type of pigments in which the element that gives the colouration (named chromophore) penetrates into the crystalline structure of a metallic oxide (which is the host substance). In many cases, a third metallic oxide is used to ensure the presence of a counterion that guarantees electroneutrality balance within the mixture. A flux may also be used to promote species mobility and thus reducing the reaction temperature.

The method of production can vary depending on the type of pigment to be produced. In the ceramic method, one of the most used in the pigment sector, the raw material comprising of several metal oxides is heated continuously in a rotary kiln until it decomposes thermally and suffers calcination. The temperatures are high to improve mobility and reactivity of the chemical species [2] and the heating source is typically a hot gas flowing in the reactor and exchanging heat with the solids by convection. This hot gas generally results from the combustion of a fossil fuel.

In the present days, pigments are used worldwide. The high quantities of pigments produced, as well as the high temperatures needed for their production, make the pigment sector a very energy intensive one, which can be aggravated by the low efficiencies of the conventional processes. Consequently, the pigment sector contributes to a very high level of greenhouse gas (GHG) emissions, because the heating source depends extensively on fossil fuels. As such, microwave heating has became one of the most popular heating sources because of the zero direct GHG emissions associated to it.

Microwave heating, as a volumetric phenomenon, is more rapid and allows a higher temperature uni-

formity if the electric field penetrates the material, is less energy demand and is much more controllable when compared to conventional heating [3]. Electromagnetic heating is a consequence of the rotation of molecules having a non-zero dipolar moment when an external electric field is applied, and thus producing heat due to the presence of friction [3]. Joule effect may also play a role when the material is a conductor. The electromagnetic heat source will depend on the applied electric field and the complex permittivity of the material, specially its imaginary part, which determines the amount of heat dissipated in the material.

There are a few disadvantages of microwave processing concerning heating uniformity when there is significant attenuation of the electric field within the material. If the complex permittivity is too high, the electric energy dissipates in the material as heat and the electric field vanishes as it propagates in the load. The penetration depth (δ), given by the distance at which the electric field drops to $1/e$ (about 37%) of its value in the material surface, is a measure of this attenuation. If the thickness of the load is much higher than δ, then the heating efficiency decreases and thermal gradients may be aggravated. Thermal-runaway is another problem that may arise when the complex permittivity increase with temperature, which induce a positive feedback mechanism that is difficult to control. This mechanism appears because the increase in temperature leads to an increase in the heating source, resulting in even higher temperatures [4]. Besides this, thermal gradients are also increased, which can affect the material quality. To avoid this phenomenon, control of the input power is a mandatory strategy in microwave heating devices. These problems are more common in materials having low thermal conductivity, due to the higher resistance in the heat flow out of the hot-spots [5].

Several authors have dealt with microwave heating control. In Reference [6], a ceramic material is heated using microwaves and it is concluded that attenuation occurs significantly and there is a delay between thermal and electromagnetic interfaces. Glass production using microwaves is addressed in Reference [7], where an automatic impedance control is achieved by changing the cavity length for microwave efficiency optimization. Concerning microwave heating of pigments, small amounts of $(Pr, Zr)SiO_4$ were produced in Reference [8], requiring pre-heating to start dielectric response of materials. Nevertheless, chemical conversion is slow and unsatisfactory, which cause small colour change. In Reference [9], non-doped TiO_2 is produced and it is concluded that microwaves promote anatase to rutile phase transformation and reduce the temperature of this transformation.

Concerning the conventional process, the mechanism of formation of zircon silicate is studied in Reference [10], where it was concluded that the flux is responsible for the formation of a melted phase that facilitates the migration of Si^{4+} to the ZrO_2 structure. This mechanism was also confirmed for the Pr-doped pigment [11, 12]. The influence of Sb_2O_3 in the anatase to rutile transformation was studied in Reference [13] and an identical study was conducted in Reference [14] including more combinations of chromophores and counterion species. Both works conclude that Cr_2O_3 and Sb_2O_3 promote phase transformation from anatase to rutile. The production of pigments in a rotary kiln was addressed in References [15, 16] for non-doped TiO_2.

Regarding chemical kinetic analysis, one of the fields of this work, model-fitting and model-free methods were compared in Reference [17] for isothermal and non-isothermal data. A model-fitting approach was used to model the phase transformation from anatase to rutile in Reference [18] using a JMAK model (known as Avrami equation). In Reference [19], the Coats-Redfern equation was used to determine Arrhenius parameters for the decomposition of metatitanic acid, one of the reactions that occur in the production of TiO_2 white pigment.

The objective of this Thesis is to build a mathematical model for the continuous production of ceramic pigments having microwaves as heat source. The model was built using *COMSOL Multiphysics*, due to its versatility at combining different physics and equations in the same model. It will be conducted a parametric study of some operational variables, allowing a better insight into this heating process and improving its efficiency. To accomplish this goal, a numerical controller was built in *MATLAB* to minimize temperature related problems. Solution Verification was also included to increase the results reliability.

2. Background

2.1. Chemical model

In solid state kinetics, it is common to define the reaction rate by equation (1) for a isothermal experiment and by equation (2) for a non-isothermal one. The reaction constant is defined in equation (3), using an Arrhenius temperature dependence.

$$\frac{d\alpha}{dt} = k(T)f(\alpha) \tag{1}$$

where α is the conversion degree, t is the time [s], k is the reaction constant [s^{-1}], T is the temperature [K] and $f(\alpha)$ is the kinetic model.

$$\frac{d\alpha}{dT} = \frac{k(T)}{\beta}f(\alpha) \tag{2}$$

where $\beta = dT/dt$ is the heating rate [K/s].

$$k(T) = k_0 \exp\left(-\frac{E_a}{RT}\right) \tag{3}$$

where k_0 is the pre-exponential factor [s^{-1}], E_a is the activation energy [J/mol] and $R = 8.314\,\mathrm{J/(mol\,K)}$ is the universal gas constant.

The set of variables k_0, E_a and $f(\alpha)$ is named the kinetic triplet, which was determined using a model-fitting method. To conduct this approach, it is necessary to choose an appropriate reaction model. JMAK model, given by equation (4), also known as Avrami equation, was used following the procedure taken by Reference [18].

$$\alpha(t) = 1 - \exp[-(kt)^n] \tag{4}$$

where n is the Avrami exponent.

The kinetic model is given by equation (5) and the integrated kinetic model is showed in equation (6).

$$f(\alpha) = n\,(1-\alpha)[-\ln(1-\alpha)]^{1-\frac{1}{n}} \tag{5}$$

$$g(\alpha) = \int_{\alpha_0}^{\alpha} \frac{d\tilde{\alpha}}{f(\tilde{\alpha})} = [-\ln(1-\alpha)]^{\frac{1}{n}} \tag{6}$$

where $g(\alpha)$ is the integrated kinetic model.

The reaction constant and Avrami exponent may be determined from an isothermal experiment using equation (7) and the line that better fits the experimental points $(\ln(t_i), \ln[-\ln(1-\alpha_i)])$. The same procedure may be repeated for a non-isothermal one with equation (8), which is Coats-Redfern equation.

$$\ln[-\ln(1-\alpha)] = n\ln(k) + n\ln(t) \tag{7}$$

$$\ln\left[\frac{g(\alpha)}{T^2}\right] = \ln\left[\frac{k_0 R}{\beta E_a}\left(1 - \frac{2R\bar{T}}{E_a}\right)\right] - \frac{E_a}{RT} \tag{8}$$

where $\bar{T}$ is an average temperature of the non-isothermal experiment.

The Arrhenius parameters (k_0 and E_a) can be determined from the dependence of the reaction constant with temperature using equation (9).

$$\ln[k(T)] = \ln(k_0) - \frac{E_a}{RT} \tag{9}$$

The described model-fitting approach assumes a single step mechanism for the chemical conversion. The obtained Arrhenius parameters can only be used together with the assumed reaction model and do not have useful physical meaning.

The chemical species transport phenomenon is modelled by equation (10), which includes convection and occurrence of chemical reactions, while assuming no diffusion transport. Equation (10) was solved for α assuming stationary regime ($\partial/\partial t = 0$) and setting $R = \rho k(T) f(\alpha)$, giving a similar result to equation (1).

$$\rho\frac{\partial \omega_i}{\partial t} + \rho(\mathbf{v}\cdot\nabla\omega_i) = R_i \tag{10}$$

where i is the species index, ρ is the density [$\mathrm{kg/m^3}$], ω is the mass fraction, $\mathbf{v}$ is the velocity vector [m/s] and R is the chemical species source from chemical reactions [$\mathrm{kg/m^3\,s}$].

2.2. Thermal model

Heat transport phenomenon is described by the energy equation (equation (11)), that includes heat convection and conduction within the material.

$$\frac{\partial}{\partial t}(\rho C_p T) + \mathbf{v}\cdot\nabla(\rho C_p T) + \nabla\cdot\dot{\mathbf{q}}'' = Q \tag{11}$$

where C_p is the specific heat at constant pressure [J/(kg K)], $\dot{\mathbf{q}}''$ is the heat flux [$\mathrm{W/m^2}$] and Q is the heat source [$\mathrm{W/m^3}$] – for example, provided by electromagnetic heating. The heat flux is given by the Fourier Law of conduction: $\dot{\mathbf{q}}'' = -k\nabla T$, where k is the thermal conductivity [W/(mK)].

An energy balance was performed to verify the results of the thermal interface and monitor the heat flows in the domain. The energy balance is given in the set of equations (12) and is formally given by equation (12a).

$$B_1 + B_2 - B_3 - B_4 = 0 \tag{12a}$$

$$B_1 = \iiint_{\mathrm{VC}} \mathbf{v}\cdot\nabla(\rho C_p T)\,dV \tag{12b}$$

$$B_2 = \iint_{\mathrm{SC_1}} h(T - T_{\mathrm{ext}})\,dA + \iint_{\mathrm{SC_2}} (-k\nabla T)\cdot\hat{\mathbf{n}}\,dA \tag{12c}$$

$$B_3 = \dot{Q}_{EM} \tag{12d}$$

$$B_4 = \iiint_{\mathrm{VC}} |\mathbf{v}\cdot\nabla\alpha|\,(-\Delta H)\,\rho\,dV \tag{12e}$$

where h is the convection coefficient [$\mathrm{W/(m^2K)}$] in the boundaries where heat exchange through convection was prescribed (given by SC_1; SC_2 are the remaining boundaries), $T_{ext} = 293.15\,\mathrm{K}$ is the exterior temperature, $\hat{\mathbf{n}}$ is the exterior normal, $\dot{Q}_{EM}$ is the electromagnetic heat source [W] and ΔH is the enthalpy of reaction [J/kg].

2.3. Electromagnetic model

Electromagnetic field can be described by Maxwell's equations, presented in equation set (13). Constitutive relations are given by equations (14), where equation (14c) is Ohm's Law.

$$\nabla \times \mathbf{E} = -\frac{\partial \mathbf{B}}{\partial t} \tag{13a}$$

$$\nabla \times \mathbf{H} = \frac{\partial \mathbf{D}}{\partial t} + \mathbf{J} \tag{13b}$$

$$\nabla \cdot \mathbf{D} = \rho_c \tag{13c}$$

$$\nabla \cdot \mathbf{B} = 0 \tag{13d}$$

where $\mathbf{E}$ is the electric field [V/m], $\mathbf{B}$ is the magnetic flux density [Wb/m^2], $\mathbf{H}$ is the magnetic field [A/m^2], $\mathbf{D}$ is the electric flux density [C/m^2], $\mathbf{J}$ is the electric current density [A/m^2] and ρ_c is the electric charge density [C/m^3].

$$\mathbf{D} = \epsilon \mathbf{E} \tag{14a}$$

$$\mathbf{B} = \mu \mathbf{H} \tag{14b}$$

$$\mathbf{J} = \sigma \mathbf{E} \tag{14c}$$

where $\epsilon = \epsilon' - j\epsilon''$ is the electric permittivity [F/m], $\mu = \mu' - j\mu''$ is the magnetic permeability [H/m] and σ is the electric conductivity [S/m] of the material.

Combining Maxwell's equations with constitutive relations, one obtains Helmholtz equation (equation (15)), which is solved for the vectorial field $\mathbf{E}$.

$$\nabla \times \frac{1}{\mu_r}(\nabla \times \mathbf{E}) - k_0^2 \left(\epsilon_r - \frac{j\sigma}{\omega \epsilon_0} \right) \mathbf{E} = 0 \tag{15}$$

The quantities ϵ and μ can be complex numbers. Its real part accounts for the ability of the materials to store electric (ϵ) or magnetic (μ) energy, while the imaginary part is related to the attenuation of electric or magnetic dipole moments within the material. These attenuations are responsible for the heat generation, which means that a material susceptible of being heated by microwaves must have a non-zero permittivity and/or permeability imaginary part. In the present case, attenuation of magnetic dipole moments was neglected ($\mu'' = 0$) and the heat source is thus given by equation (16).

$$\dot{Q}_{\mathrm{EM}} = \int_{\mathrm{VC}} \frac{\sigma}{2} |\mathbf{E}|^2 \, dV + \int_{\mathrm{VC}} \frac{\omega \epsilon''}{2} |\mathbf{E}|^2 \, dV \tag{16}$$

where $|\mathbf{E}|$ is the electric field norm [V/m^2] and ω is the angular frequency [rad/s].

2.4. Coupling

There is a major dependency between the three interfaces introduced. The dielectric properties change with temperature and the electromagnetic heat source has to be considered in the energy equation. Besides this, temperature influences the reaction constant (equation (3)) and the chemical reactions release heat (equation (12e)). These major dependencies are summarized in figure 1.

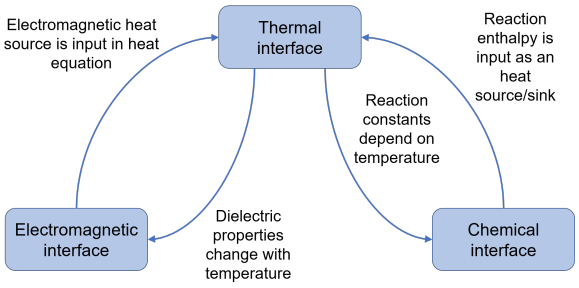

Figure 1: Dependencies between physical interfaces.

3. Validation and Verification

A Validation/Verification study was conducted using the Grid Convergence Index (GCI) method. It was assumed that discretization error dominates numerical one and follows a power series expansion evolution of the form of equation (17), which is valid in the asymptotic regime.

$$\epsilon_i = \phi_i - \phi_0 = \alpha h_i^p \tag{17}$$

where ϵ is the discretization error, ϕ is a control variable, α is a constant to be determined, h is a characteristic element length [m], p is the observed order of convergence and i is the mesh index, that decreases with mesh refinement.

An estimated value for zero size grid can be obtained using Richardson extrapolation (ϕ_R), which is given by:

$$\phi_0 \approx \phi_R = \phi_1 + \frac{\phi_1 - \phi_2}{r_{21}^p - 1} + O(h^{p+1}) \tag{18}$$

where $r_{21} = h_2/h_1$ is the refinement ratio.

The order of convergence can be calculated using the non-linear equation (19) and the GCI for the 2 most refined grids can be evaluated using equation (20). Numerical uncertainty is calculated by setting $U_{num} = GCI_{12}$ [20].

$$\frac{\phi_1 - \phi_2}{\phi_2 - \phi_3} = \left(\frac{h_1}{h_2} \right)^p \left(\frac{\left(\frac{h_2}{h_1} \right)^p - 1}{\left(\frac{h_3}{h_2} \right)^p - 1} \right) \tag{19}$$

$$GCI_{12} = \frac{F_s}{r_{21}^p - 1} \left| \frac{\phi_1 - \phi_2}{\phi_1} \right| \tag{20}$$

where F_s is a factor of safety.

3.1. Yellow pigment

Yellow pigment has a nominal composition given by $Zr_{1-x}Pr_xSiO_4$ and is produced by the following chemical reaction:

$$(1-x)\,ZrO_2 + SiO_2 + \frac{x}{6}\,Pr_6O_{11} + \frac{x}{12}\,O_2 \rightarrow P \quad (21)$$

where $x = 0.0189$ is the doping fraction and $P = Zr_{1-x}Pr_xSiO_4$ is the product.

Equation (7) was used to predict kinetic parameters from the isothermal data present in [12]. The results are presented in table 1, where it is possible to conclude that there is a major dependency of the reaction constant and Avrami exponent on temperature. Reaction constant increases with temperature due to higher reactivity and the R^2 values are close to unity, indicating an adequate fit with experimental results. The fact that different Avrami exponents were obtained at low temperatures is consistent with the different kinetic models proposed by [12] at those temperatures.

Table 1: Results obtained for the kinetic analysis of the experimental data in [12] (yellow pigment).

$T\ [°C]$	$k\ [s^{-1}]$	n	R^2
750	3.96×10^{-5}	3.71	0.9896
800	4.54×10^{-5}	2.81	0.9955
850	1.13×10^{-4}	1.98	0.9875
900	1.30×10^{-4}	1.95	0.9971
1000	2.71×10^{-4}	2.05	0.9978

Arrhenius parameters were obtained using equation (9), leading to $k_0 = 1.09319\,s^{-1}$ and $E_a = 87\,754.27$ J/mol. The obtained $R^2 = 0.952$ indicates that k follows closely an Arrhenius evolution. Nevertheless, using equation (3) can induce errors up to 30% in the prediction of the reaction constants in the temperature range $800 - 900\,°C$.

After the kinetic triplet is known, it is possible to reproduce isothermal conversion using equation (1). The results are presented in figure 2, where it is possible to see excellent agreement with the experimental data.

Table 2 summarizes the results obtained for Solution and Code Verification. The observed order of convergence is pretty close to the theoretical one (which is 2, because quadratic elements were used to discretize the convection term). Consequently, Code Verification is accomplished with success. Moreover, it is possible to conclude that the error associated with the third most refined mesh is low and only about 10 times greater than the one obtained with the finer mesh. As such, the third most refined grid ($h_3 = 1.25 \times 10^{-3}$ m) was used to present the results. Numerical uncertainty is less than 0.01% for both heating rates.

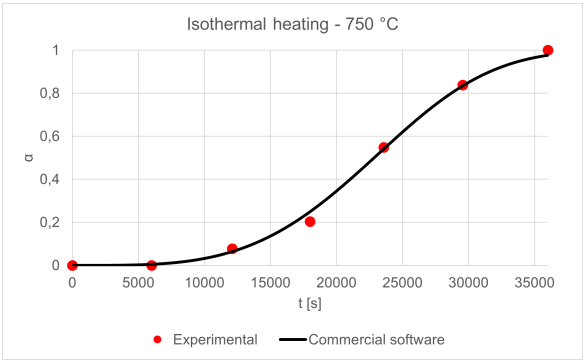

(a) 750 $°C$

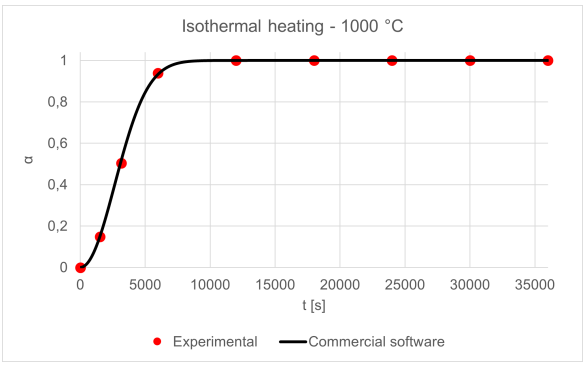

(b) 1000 $°C$

Figure 2: Obtained results for the isothermal conversion simulations (yellow pigment). Simulation time was 600 minutes.

Table 2: Results obtained for Solution and Code Verification (yellow pigment).

Parameter	3 K/min	0.5 K/min
ϕ_R	0.0863030899	0.259187774
p	1.9707	1.9441
GCI_{23}	3.00×10^{-5}	1.03×10^{-4}
$GCI_{12} = U_{num}$	7.59×10^{-6}	2.61×10^{-5}
ϵ_3	8.10×10^{-6}	8.13×10^{-5}
ϵ_1	5.18×10^{-7}	5.28×10^{-6}

3.2. Brown pigment

The nominal composition of brown pigment is $Ti_{1-2x}Cr_xSb_xO_2$ and its reaction is given by

$$(1-2x)\,TiO_{2(a)} + \frac{x}{2}\,Sb_2O_3 + \frac{x}{2}\,Cr_2O_3 + \frac{x}{2}\,O_2 \rightarrow P \quad (22)$$

where a stands for anatase phase, r for rutile phase and $P = Ti_{1-2x}Cr_xSb_xO_{2(r)}$ is the product.

Equation (8) was used to extract Arrhenius parameters from non-isothermal data obtained by

Reference [14]. Model-fitting method requires the knowledge of Avrami exponent when non-isothermal data is used. So, among several values, $n = 1.5$ was chosen, leading to $k_0 = 4.54 \times 10^3\,\mathrm{s}^{-1}$ and $E_a = 1.44 \times 10^5\,\mathrm{J/mol}$. Other combinations of n, k_0 and E_a could be obtained as kinetic analysis is being made using non-isothermal data obtained at one single heating rate.

Non-isothermal conversion profiles were simulated via commercial software and the simplest closed Newton-Cotes integration rule. The results are presented in figure 3, together with experimental results for $\beta = 200\,\mathrm{K/h}$, and show a very good agreement between experimental and simulated curves. Note that numerical results obtained with commercial software and integration rule are indistinguishable.

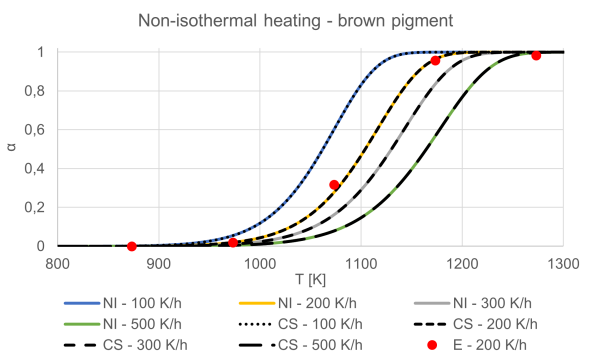

Figure 3: Results obtained for the non-isothermal heating (brown pigment): NI stands for Numerical Integration, CS for Commercial Software and E for Experimental.

Table 3 summarizes the results obtained during Verification. The observed order of convergence is different from the theoretical one due to the inadequate boundary condition used, which prescribes $d\alpha/dT = 0$ at the final temperature. This inadequacy is higher at lower heating rates, justifying the lower value of p at $\beta = 200\,\mathrm{K/h}$. However, the obtained p is close to the theoretical one ($p = 2$) for $\beta = 500\,\mathrm{K/h}$ and numerical uncertainty is very low, as well as the absolute error, which decreases only slightly for the three most refined grids. Numerical uncertainty is higher than absolute error, as expected.

4. Mathematical model

2D and 3D geometries were tested in the present model and are shown in figure 4. The rectangular cavity is filled with air at ambient pressure and is penetrated by a circular tube where the material flows and is heated. In the 2D geometry, the tube is completely filled with material while in the 3D study a filling angle of 120° was used. The WR-340 waveguide operates at single TE_{10} mode and a frequency of 2.45 GHz.

Table 3: Results obtained for Solution and Code Verification (brown pigment).

Parameter	500 K/h	200 K/h
ϕ_R	0.285127761	0.404776707
p	2.0527	1.8486
GCI_{23}	1.77×10^{-6}	6.90×10^{-6}
$GCI_{12} = U_{num}$	3.73×10^{-7}	1.91×10^{-6}
ϵ_3	1.61×10^{-6}	8.04×10^{-6}
ϵ_1	7.15×10^{-8}	6.18×10^{-7}

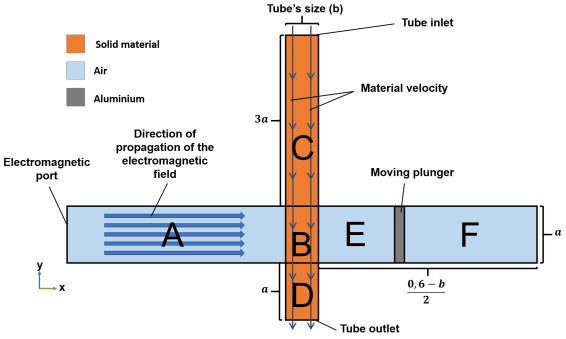

(a) $2D$

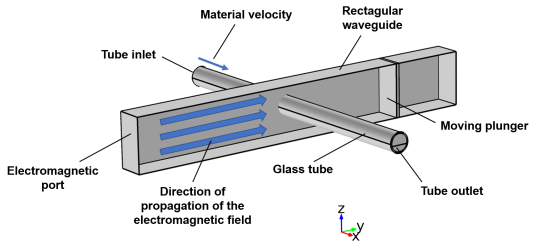

(b) $3D$

Figure 4: Schematic representation of the cavities used in the model.

The moving plunger allows for the control of the cavity impedance by varying its length. The amplitude of the moving plunger was chosen to be greater than the electric field local wavelength (173 mm), allowing the occurrence of at least one peak of electromagnetic efficiency. Initial conditions include $\alpha = 0.001$, $\mathbf{E} = \mathbf{0}$ and a linear temperature profile between the tube inlet ($T = 300\,\mathrm{K}$) and the cavity outlet ($T = 1200\,\mathrm{K}$ for yellow pigment and $T = 900\,\mathrm{K}$ for brown one). For the electromagnetic interface, perfect electric conductor was assigned to every boundary (except the port) as well as convective heat transfer in the thermal interface (except at the inlet and outlet). For the convection coefficient at the boundaries free convection correlations

from Reference [21] were used in the 3D case.

Density was assigned constant and equal to the value for the stoichiometric mixture of reactants (equation (23)), while specific heat was calculated using equations (24) and (25). Temperature dependent values for C_p were extracted from Reference [22]. Conductivity values used were: $k_{yellow} = 3.5\,\mathrm{W/(m\,K)}$ and $k_{brown} = 0.5\,\mathrm{W/(m\,K)}$.

$$\rho_m = \left(\sum_{i=1}^{N} \frac{Y_i}{\rho_i} \right)^{-1} \tag{23}$$

where m stands for mixture, Y is the mass fraction, and i is the species' index.

$$C_{p,m} = \sum_{i=1}^{N} Y_i C_{p,i} \tag{24}$$

$$C_p = (1-\alpha)\, C_{p,R} + \alpha\, C_{p,P} \tag{25}$$

where R stands for the reactants mixture and P for the product.

To maximize electromagnetic efficiency and avoid temperature related problems, power and plunger position were controlled with a *MATLAB* routine, whose algorithm is presented next. The input power was calculated using equation (26).

$$P_{\mathrm{port}} = \frac{1}{\eta_{EM}} [B_1 + B_2 - 0.999\,\dot{m}\,(-\Delta H)] \tag{26}$$

where the convective term B_1 is calculated with equation (12b), the thermal losses term B_2 is determined using equation (12c) and $\dot{m}$ is the mass flow rate [kg/s].

1. Introduce input variables: velocity, boundary convection coefficient and simulation time (15% of the residence time inside the cavity).
2. Perform a parametric study regarding plunger position to determine the electromagnetic maximum efficiency and the associated plunger position for the initial temperature field.
3. Assign the plunger position and electromagnetic efficiency to the values calculated in 2.
4. Simulations cycle:
   (a) Run simulation, using equation (26) to determine the input power.
   (b) Extract a list of useful control variables to analyse the results.
   (c) Stopping conditions testing cycle:
      i. Transient term less than 3% of absorbed power and conversion degree higher than 0.99: simulation stops, go to 5;
      ii. Otherwise: simulation proceeds.
   (d) Cycle to determine the new plunger position that guarantees maximum efficiency:
      i. Test actual position and the two adjacent positions (left and right):
         A. Maximum efficiency in the central position: store the efficiency and plunger position values; go to 4-e;
         B. Otherwise: from the 3 positions, the one that guarantees maximum efficiency is set to be the central one; go back to 4-d-i.
   (e) Update plunger position and electromagnetic efficiency values and go back to 4-a;
5. Create a table with the evolution of control variables with time.

5. Results

Non-zero complex permittivity allows the material to heat but has the drawback of making the electric field being attenuated in the load, decreasing the heating efficiency. As such, there has to be a compromise between efficiency and mass flow rate in a 2D study, as the tube diameter for which efficiency is maximum is close to 2.5 mm. High diameters should also be avoided because of the superficial nature of electromagnetic heating when complex permittivity is high, leading to low temperature zones when the electric field is significantly attenuated (specially if the thermal conductivity is low). The low values of penetration depth obtained (less than 1 mm) are an indicator of the non-volumetric heating.

As dielectric properties increase with temperature, penetration depth decreases and the heating becomes even more superficial (figures 5b and 5c): the heating source becomes higher but its volume decreases, leading to a decrease in efficiency. Consequently, maximum temperature increase but the average one decreases – figure 6. As such, electromagnetic heating of materials having high or temperature increasing dielectric properties and low thermal conductivity can be a problem if a certain temperature is to be reached in every area of the load – as happens when chemical reactions are occurring. Superficial heating may thus slow down reaction kinetics far away from the surface and limit the velocities of the material to very low values. When the reactions occurring are exothermic, there is a special enhancement of superficial heating phenomena as those reactions only occur where temperature is above a certain value, *i.e.*, energy release will occur where temperature is higher, aggravating the superficial heating.

The reduced initial temperature for brown pigment, together with lesser dielectric properties and

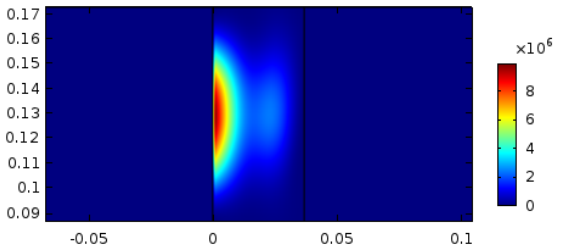

(a) Yellow pigment – $t = 0\,s$

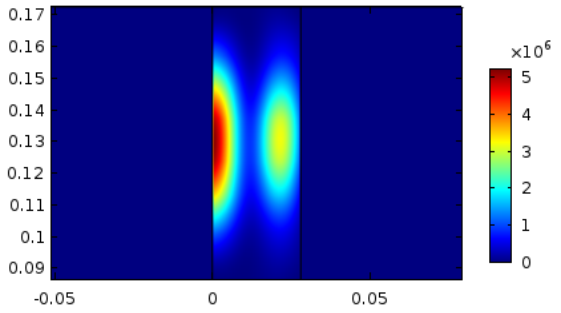

(b) Brown pigment – $t = 0\,s$

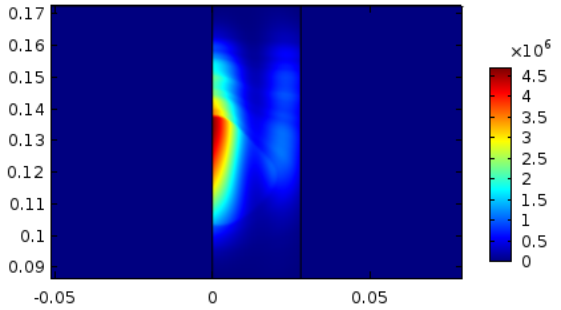

(c) Brown pigment – $t = 2590.8\,s$

Figure 5: Initial heat source distribution $[W/m^3]$ for both pigments.

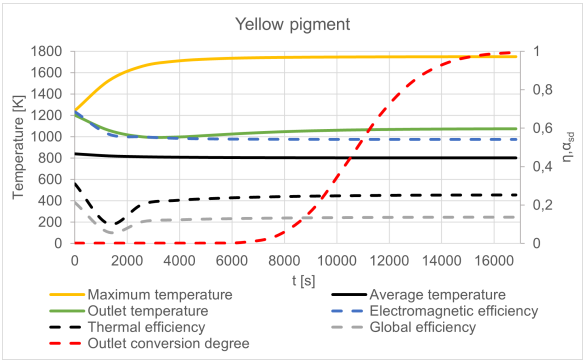

(a) Yellow pigment

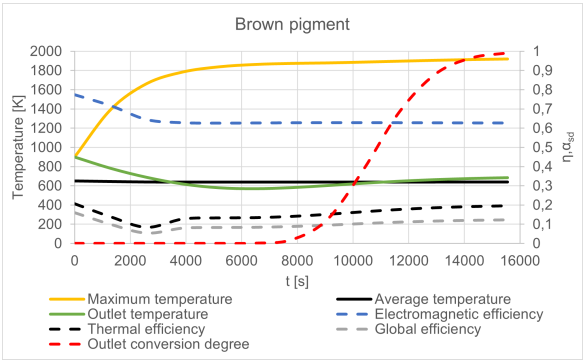

(b) Brown pigment

Figure 6: Convergence history for both pigments.

a smaller tube, lead to a less significant attenuation of the electromagnetic heat source in the tube (figures 5a and 5b) and improved electromagnetic efficiency (figure 6). Reducing initial temperature and tube diameter can thus improve heating uniformity and promote volumetric heating.

Although brown pigment has a smaller complex permittivity (that makes the heat source less intense – figure 5), its smaller thermal conductivity leads to a higher maximum temperature, because thermal losses are inhibited. Smaller conductivity also makes the difference between maximum and average temperatures higher for the brown pigment – figure 6.

Using a smaller tube leads to more plunger position updates, since the electric field attenuation in the tube is smaller. As such, the electric field norm in the area between the load and the moving plunger is higher for the smaller tube diameters, for which there is much more benefit in having a moving plunger.

The maximum temperature increases with material velocity (figure 7) as more material is being subjected to electric field and the heating is volumetric. The increase in convection coefficient makes maximum temperature increase, which may seem erroneous. The explanation is related to power control and equation (26): heating losses are being accounted in the input power, which means that higher thermal losses lead to higher input power. As heating is superficial and the heating zone is not close to the boundaries, the heat is released far away from where it is generated, leading to a positive local energy balance that makes maximum temperature to increase. The fact that non-volumetric effects are aggravated by the increase in maximum temperature creates a positive feedback mechanism that makes that tendency even stronger. Note that global energy balance is always net zero but the local one may not be as it is impossible to give heat in the same areas where it is released. This is also why a convection coefficient parametric study was performed in this work. These results clearly show that thermal insulation must be carried out not only for efficiency promotion but also to reduce the maximum temperature in the solid bed (increasing convection coefficient to reduce temperature field would have the opposite effect in this context).

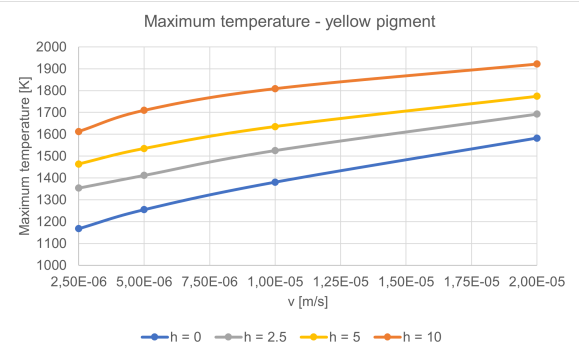

Figure 7: Maximum temperature evolution with velocity and convection coefficient for yellow pigment.

Maximum temperature should be as low as possible as long as chemical conversion occurs completely because high temperatures lead to low electromagnetic efficiencies, as electric field is more attenuated at those higher temperatures (figures 5 and 6).

Thermal efficiency increases with velocity (figure 8), suggesting that higher velocities should be tested for efficiency maximization. However, increasing velocity leads to a decrease in residence time that may become inferior to reaction time, in which case total conversion is impossible to occur.

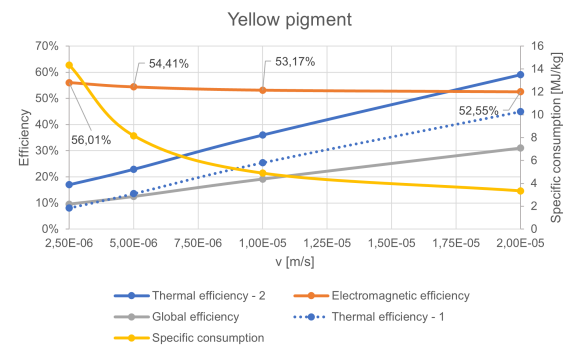

(a) Yellow pigment – $h = 10\,W/(m^2K)$

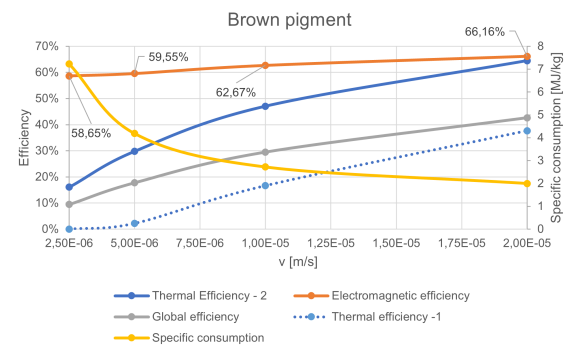

(b) Brown pigment – $h = 10\,W/(m^2K)$

Figure 8: Efficiencies and specific consumption evolution with velocity.

Non-uniform heating makes the difference between average and maximum temperatures higher due to superficial phenomena and low thermal conductivity. As maximum temperature is limited by materials' thermal limit, average temperature decreases with the increase of non-uniformity, increasing the reaction time and decreasing the maximum velocity. Promoting mixing in the bed contributes to diminish such non-uniformities in the temperature field, which benefits thermal efficiency and production rate. Heterogeneous heating spoils global efficiency and production rate.

Thermal conductivity (k) also affects thermal losses dependency with velocity: for high values of k, thermal losses are pratically constant with velocity but for lower k values, diffusive fluxes lose importance and convective fluxes become preponderant. As such, for lower k, thermal losses increase with velocity (because thermal gradients increase with velocity). Consequently, electromagnetic efficiency increases with velocity for brown pigment but has an opposite evolution for yellow pigment (figure 8). Thermal efficiency also benefits with a smaller k because thermal losses decrease. Global efficiency is thus higher for brown pigment (figure 8).

6. Conclusions

The controller developed in *MATLAB* was able to successfully avoid temperature related problems, such as thermal-runaway and hot-spots. The results show that it is possible to produce ceramic pigments using microwaves while having efficiencies around 60%.

Electromagnetic heating of materials having high dielectric permittivity and low thermal conductivity can be a challenge because of the heterogeneous heating. This is a consequence of superficial heating caused by attenuation of the electric field within the material. When chemical conversion is to be considered, these problems become more important as kinetic evolution is highly dependent on temperature.

The present results show the importance of promoting solids mixing, as this contributes to lesser temperature gradients and allow for higher velocities, while guaranteeing total conversion. The increase in thermal efficiency and production rate is the main advantage.

Finally, electromagnetic heating can be a sustainable alternative to the conventional one as it allows a significant reduction in GHG specific emissions.

References

[1] G. Buxbaum and G. Pfaff, editors. *Industrial Inorganic Pigments*. Wiley-VCH, 3rd edition, 2005.

[2] G. Pfaff, editor. *Inorganic Pigments*. De Gruyter, 1st edition, 2017.

[3] S. Das, Anoop Mukhopadhyay, Someswar Datta, and D. Basu. Prospects of microwave processing: An overview. *Bulletin of Materials Science*, 32(1):1–13, Dezembro 2009.

[4] Xiang Zhao, Liping Yan, and Kama Huang. Review of numerical simulation of microwave heating process. In Stanisław Grundas, editor, *Advances in Induction and Microwave Heating of Mineral and Organic Materials*, chapter 2, pages 27–48. InTech, 2011.

[5] Roger Meredith, editor. *Engineers' Handbook of Industrial Microwave Heating*. The Institution of Electrical Engineers, 1st edition, 1998.

[6] T. Santos, M.A. Valente, J. Monteiro, J. Sousa, and L.C. Costa. Electromagnetic and thermal history during microwave heating. *Applied Thermal Engineering*, 31(16):3255–3261, 2011.

[7] Ricardo M.C. Mimoso, Duarte M.S. Albuquerque, José M.C. Pereira, and José C.F. Pereira. Simulation and control of continuous glass melting by microwave heating in a single-mode cavity with energy efficiency optimization. *International Journal of Thermal Sciences*, 111:175–187, 2017.

[8] M. Blosi, M. Dondi, S. Albonetti, G. Baldi, A. Barzanti, and C. Zanelli. Microwave-assisted synthesis of Pr–ZrSiO4, V–ZrSiO4 and Cr–YAlO3 ceramic pigments. *Journal of the European Ceramic Society*, 29(14):2951–2957, 2009.

[9] Yasuro Ikuma, Takashi Shigemura, and Takashi Hirose. Temperature profile of anatase-TiO2 powder compact during microwave heating. *Journal of the American Ceramic Society*, 79(10):2533–2538, 1996.

[10] R. A. Eppler. Mechanism of formation of zircon stains. *Journal of the American Ceramic Society*, 53(8):457–462, 1970.

[11] R. A. Eppler. Formation of praseodymium-doped zircon colors in presence of halides. *Industrial & Engineering Chemistry Product Research and Development*, 10(3):352–355, 1971.

[12] M. Trojan. Synthesis of a yellow zircon pigment. *Dyes and Pigments*, 9(4):261–273, 1988.

[13] Richard Eppler. Effect of antimony oxide on the anatase-rutile transformation in titanium dioxide. *Journal of the American Ceramic Society*, 70:C-64–C-66, 1987.

[14] F. Matteucci, G. Cruciani, M. Dondi, and M. Raimondo. The role of counterions (Mo, Nb, Sb, W) in Cr-, Mn-, Ni- and V-doped rutile ceramic pigments: Part 1. Crystal structure and phase transformations. *Ceramics International*, 32(4):385–392, 2006.

[15] T. Ginsberg and M. Modigell. Dynamic modelling of a rotary kiln for calcination of titanium dioxide white pigment. *Computers and Chemical Engineering*, 35(11):2437–2446, 2011.

[16] A. Agrawal and P.S. Ghoshdastidar. Numerical simulation of heat transfer during production of rutile titanium dioxide in a rotary kiln. *International Journal of Heat and Mass Transfer*, 106:263–279, 2017.

[17] Sergey Vyazovkin and Charles A. Wight. Model-free and model-fitting approaches to kinetic analysis of isothermal and nonisothermal data. *Thermochimica Acta*, 340-341:53–68, 1999.

[18] K. Lubkowski, B. Kic, B. Grzmil, and M. Gleń. Study of the anatase to rutile transformation kinetics of the modified TiO2. *Polish Journal of Chemical Technology*, 15(2):73–80, 2013.

[19] K. Przepiera and A. Przepiera. Thermal transformations of selected transition metals oxyhydroxides. *Journal of Thermal Analysis and Calorimetry*, 74(2):659–666, 2003.

[20] The American Society of Mechanical Engineers. *Standard for Verification and Validation in Computational Fluid Dynamics and Heat Transfer*, 2009.

[21] Theodore L. Bergman, Adrienne S. Lavine, P. Frank Incropera, and David P. Dewitt. *Fundamentals of Heat and Mass Transfer*. John Wiley and Sons, 7th edition, 2011.

[22] W.F. Gale and T.C. Totemeir, editors. *Smithells Metals Reference Book*. Elsevier, 8th edition, 2004.